

# Hybrid Improper Ferroelectricity in (Sr,Ca)SnO and Beyond Universal Relationship between Ferroelectric Transition Temperature and Tolerance Factor in n = 2 Ruddlesden-Popper Phases

Suguru Yoshida, Hirofumi Akamatsu, Ryosuke Tsuji, Olivier Hernandez, Haricharan Padmanabhan, Arnab Sen Gupta, Alexandra S Gibbs, Ko Mibu, Shunsuke Murai, James M Rondinelli, et al.

▶ **To cite this version:**

Suguru Yoshida, Hirofumi Akamatsu, Ryosuke Tsuji, Olivier Hernandez, Haricharan Padmanabhan, et al.. Hybrid Improper Ferroelectricity in (Sr,Ca)SnO and Beyond Universal Relationship between Ferroelectric Transition Temperature and Tolerance Factor in n = 2 Ruddlesden-Popper Phases. Journal of the American Chemical Society, 2018, 140 (46), pp.15690-15700. 10.1021/jacs.8b07998 . hal-01937240

**HAL Id: hal-01937240**

**https://univ-rennes.hal.science/hal-01937240**

Submitted on 13 Dec 2018

**HAL** is a multi-disciplinary open access archive for the deposit and dissemination of scientific research documents, whether they are published or not. The documents may come from teaching and research institutions in France or abroad, or from public or private research centers.

L'archive ouverte pluridisciplinaire **HAL**, est destinée au dépôt et à la diffusion de documents scientifiques de niveau recherche, publiés ou non, émanant des établissements d'enseignement et de recherche français ou étrangers, des laboratoires publics ou privés.

# Hybrid Improper Ferroelectricity in $(Sr,Ca)_3Sn_2O_7$ and Beyond: Universal Relationship between Ferroelectric Transition Temperature and Tolerance Factor in $n$ = 2 Ruddlesden-Popper Phases

Suguru Yoshida,[†] Hirofumi Akamatsu,[‡,¶] Ryosuke Tsuji,[†] Olivier Hernandez,[∥] Haricharan Padmanabhan,[‡] Arnab Sen Gupta,[‡] Alexandra S. Gibbs,[⊥] Ko Mibu,[#] Shunsuke Murai,[†] James M. Rondinelli,[○] Venkatraman Gopalan,[‡,§] Katsuhisa Tanaka,[†] and Koji Fujita,[*,†]

[†]Department of Material Chemistry, Graduate School of Engineering, Kyoto University, Katsura Nishikyo-ku, Kyoto 615-8510, Japan

[‡]Materials Research Institute and Department of Materials Science and Engineering and [§]Department of Physics, Pennsylvania State University, University Park, PA 16802, USA

[∥]Univ Rennes, CNRS, ISCR (Institut des Sciences Chimiques de Rennes) - UMR 6226, F-35000 Rennes, France

[⊥]ISIS Pulsed Neutron and Muon Source, STFC Rutherford Appleton Laboratory, Harwell Campus, OX11 0QX, UK

[#]Department of Physical Science and Engineering, Nagoya Institute of Technology, Gokiso-cho, Showa-ku, Nagoya, 466-8555, Japan

[○]Department of Materials Science and Engineering, Northwestern University, 2220 Campus Drive, Evanston, Illinois 60208-3108, USA

ACCEPTED Manuscript

**ABSTRACT:** Hybrid improper ferroelectricity, which utilizes nonpolar but ubiquitous rotational/tilting distortions to create polarization, offers an attractive route to the discovery of new ferroelectric and multiferroic materials because its activity derives from geometric rather than electronic origins. Design approaches based on group theory and first principles can be utilized to explore the crystal symmetries of ferroelectric ground states, but in general do not make accurate predictions for some important parameters of ferroelectrics, such as Curie temperature ($T_C$). Here, we establish a predictive and quantitative relationship between $T_C$ and the Goldschmidt tolerance factor, $t$, by employing $n$ = 2 Ruddlesden-Popper (RP) $A_3B_2O_7$ as a prototypical example of hybrid improper ferroelectrics. The focus is placed on an RP system, $(Sr_{1-x}Ca_x)_3Sn_2O_7$ ($x$ = 0, 0.1, and 0.2), which allows for the investigation of the purely geometric (ionic-size) effect on ferroelectric transitions, due to the absence of the second-order Jahn–Teller active ($d^0$ and $6s^2$) cations that often lead to ferroelectric distortions through electronic mechanisms. We observe a ferroelectric-to-paraelectric transition with $T_C$ = 410 K for $Sr_3Sn_2O_7$. We also find that the $T_C$ increases linearly up to 800 K with increasing the $Ca^{2+}$ content, i.e., with decreasing the value of $t$. Remarkably, this linear relationship is applicable to the suite of all known $A_3B_2O_7$ ferroelectrics, indicating that $T_C$ correlates with the simple crystal-chemistry descriptor, $t$, based on the ionic-size mismatch. This study provides a predictive guideline for estimating $T_C$ of a given material, which would complement the group-theoretical and first-principles design approach.

## 1. INTRODUCTION

Since the discovery of ceramic $BaTiO_3$, ferroelectricity has been an attractive topic in material science and engineering due to its theoretical interest and industrial applications[1]. This field of research has long been centered on $ABO_3$ perovskites, the family members of the first ferroelectric oxide. The most common mechanism for creating perovskite ferroelectrics lies in collective ionic displacements of electronic origin, typically driven by off-centering of the $A$- and/or $B$-site cations via the second-order Jahn-Teller (SOJT) effect[2–4]. However, the SOJT effect is usually favorable for $nd^0$ transition metal cations ($Ti^{4+}$, $Nb^{5+}$, $Ta^{5+}$) or $6s^2$ post-transition metal cations ($Pb^{2+}$, $Bi^{3+}$)[5,6], and some compounds never become ferroelectric even in the presence of these SOJT-active cations[7–10]. The strict chemical requirement is problematic for the generalization of the design guidelines, making it challenging to straightforwardly synthesize $ABO_3$ ferroelectrics.

Recent theoretical work has developed a new mechanism for achieving a ferroelectric state, whereby two nonpolar structural distortions, commonly rotations or tilts of $BO_6$ octahedra, cooperatively give rise to a net polar symmetry and induce a macroscopic polarization as a by-product[11–13]. This novel mechanism, called hybrid improper ferroelectricity[11,14], is active in layered perovskite oxides like Ruddlesden-Popper (RP)[15,16] and Dion-Jacobson phases[17], and has opened a new

avenue for the rational design of ferroelectric materials[18–20]. This form of ferroelectricity should be prevalent in perovskite-related materials because the octahedral rotations/tilts are ubiquitous structural distortions[21] (which are primarily of geometric origin and are driven by the size mismatch of the constituent ions). Indeed, a number of layered perovskites have been proposed as potential hybrid improper ferroelectrics through the integrated approach of symmetry arguments and first-principles calculations[22–30], some of which have been experimentally confirmed to exhibit switchable polarization[31–38], or at least crystalize in polar structures[39–46]. One can now utilize group theory to elucidate symmetry breaking caused by given distortions and identify whether their combinations result in a polar symmetry, and then the ferroelectricity. For real technological applications, on the other hand, it is important to evaluate key parameters of ferroelectrics, including polarization, coercive field, and Curie temperature ($T_C$). But, generally, it is not straightforward to calculate these parameters, in particular $T_C$, with high precision through the group-theoretical approach and first-principles calculations[47–49].

The Goldschmidt tolerance factor, $t$, is a simple chemistry descriptor for perovskite stability, and calculated by the following equation: $t = (r_A + r_O)/\sqrt{2}(r_B + r_O)$, where $r_A$, $r_B$, and $r_O$ represent the ionic radii of $A$-site, $B$-site, and $O^{2-}$, respectively. In this paper, we study $n = 2$ RP $A_3B_2O_7$ (Figure 1a), a prototypical example of hybrid improper ferroelectrics, and establish a predictive and quantitative relationship between $T_C$ and $t$. In order to examine the pure effect of varying ionic-size mismatch on $T_C$s, we focus on $(Sr_{1-x}Ca_x)_3Sn_2O_7$ ($x$ = 0, 0.1, and 0.2), RP compounds in the absence of SOJT-active cations. $Sr_3Sn_2O_7$ was recently reported as the first ferroelectric Sn insulator with switchable electric polarization[36]; however, its ferroelectric-to-paraelectric transition was not detected up to 1035 K. The relation between the ferroelectricity and the octahedral roration/tilt has also not been clarified. Here, we successfully reveal a first-order ferroelectric-to-paraelectric transition from $A2_1am$ to $Pnab$ symmetry in $Sr_3Sn_2O_7$ ($T_C$ = 410 K, Figure 1b) using powder neutron diffraction (ND) and synchrotron X-ray diffraction (SXRD) as well as optical second harmonic generation (SHG). The experimental studies, complemented by first-principles density functional theory (DFT) calculations, allow us to identify the role played by the two nonpolar structural distortions—oxygen octahedral rotations (OOR, rotational modes about $c$ axis) and oxygen octahedral tilts (OOT, rotational modes about the $a$ and/or $b$ axis)—in stabilizing the ferroelectric $A2_1am$ and paraelectric $Pnab$ structures. Our results demonstrate that the stable ferroelectric $A2_1am$ phase appears through a trilinear coupling of OOR and OOT modes to a polar mode (i.e., hybrid improper ferroelectric mechanism) and that the metastable $Pnab$ polymorph, which competes with the equilibrium $A2_1am$ phase, emerges from a trilinear coupling of OOR and OOT modes interacting with an antipolar mode (i.e., hybrid improper antiferroelectric mechanism)[37,50,51]. Further, we observe that the $T_C$s increase linearly with the substitution of $Ca^{2+}$ for $Sr^{2+}$. Remarkably, when we consider the fifteen compounds consisting of $n$ = 2 RP ferroelectrics reported here and those reported previously ($Ca_3Ti_2O_7$[32], $Ca_3Mn_2O_7$[40], $Sr_3Zr_2O_7$[37], $(Ca,Sr)_3Ti_2O_7$[34], and $Ca_3(Ti,Mn)_2O_7$[32,35]), a simple linear relationship is found between $T_C$ and $t$, despite the diversity of chemical composition. It is surprising that the $T_C$ strongly correlates with the simple chemistry-descriptor, $t$, based on ionic-size mismatch. Our findings show the controllability of $T_C$ in hybrid improper ferroelectrics and provide a rule of thumb for predicting $T_C$s of as-yet-unsynthesized materials that would complement the group-theoretical design strategy.

## 2. METHODS

**Experimental procedures** Polycrystalline samples of $(Sr_{1-x}Ca_x)_3Sn_2O_7$ ($x$ = 0, 0.1, and 0.2) were synthesized by a solid-state reaction. Reagent-grade $SrCO_3$ (99.9%), $CaCO_3$ (99.9%) and $SnO_2$ (99.9%) were mixed so as to obtain a stoichiometric composition, ground in an agate mortar, and pressed into a pellet. The pellet was calcinated at 1000 °C for 6 h and sintered at 1300 °C for 48 h. The resultant pellet was

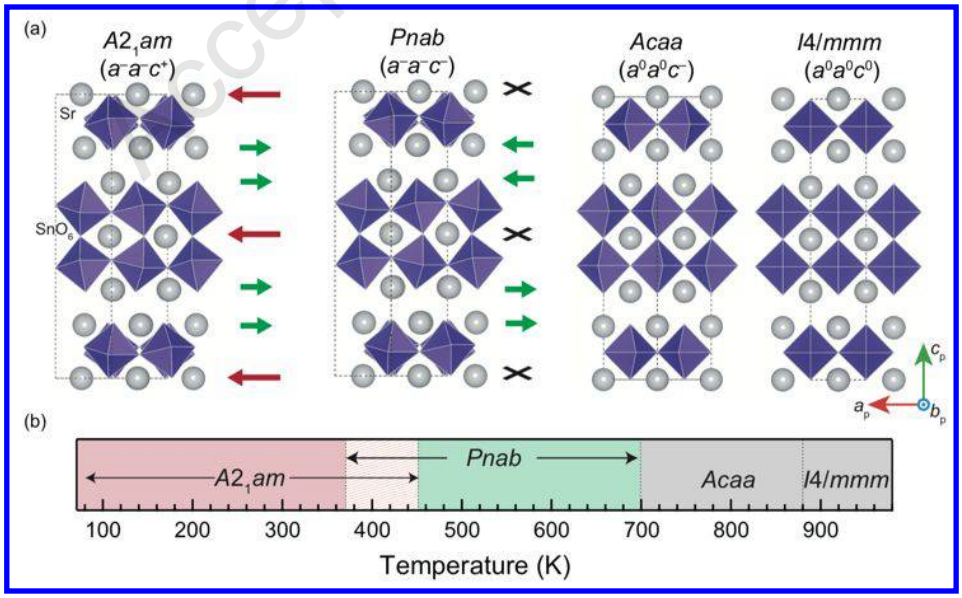



**Figure 1.** (a) The crystal structures of four phases observed experimentally for $Sr_3Sn_2O_7$ are illustrated, specified by the space group symmetry and Glazer tilt notation. Gray spheres and blue octahedra denote the Sr cations and $SnO_6$ octahedra, respectively. Black dotted lines indicate the unit cells. For $A2_1am$ and $Pnab$ phases, local electric dipoles arise from Sr cation displacements are shown by red and green arrows. Black cross marks indicate that there are no Sr displacements and thus no layer polarization. (b) The phase diagram of $Sr_3Sn_2O_7$ established in the present stu

Accepted Manuscript

ground, thoroughly mixed, pelletized again, and sintered at 1500 °C for 6 h. They were slowly cooled to room temperature.

High-resolution time-of-flight ND was performed using the HRPD diffractometer at the ISIS facility, UK; data at 300 K were collected for $(Sr_{1-x}Ca_x)_3Sn_2O_7$ ($x$ = 0, 0.1, and 0.2), and data at higher temperatures (300–950 K) were recorded for $Sr_3Sn_2O_7$ ($x$ = 0). Approximately 5 g of the finely ground powder sample was housed in a vanadium can with an inner diameter of 11 mm. Using three detection banks (backscattering bank, 90° bank, and low angle bank), we obtained diffraction patterns over a time-of-flight range of 30–130 ms corresponding to a $d$-range of 0.65–9.0 Å. For 300 and 500 K, the diffraction patterns over a time-of-flight range of 100–200 ms were also recorded to observe the Bragg reflections in the longer $d$-spacing. SXRD were carried out for $(Sr_{1-x}Ca_x)_3Sn_2O_7$ ($x$ = 0, 0.1, and 0.2) in the temperature range of 300 to 900 K using the large Debye-Scherrer camera with MYTHEN solid-state detectors installed at SPring-8 BL02B2, Japan. The incident X-ray was monochromated at $\lambda$ = 0.798833 Å or 0.800484 Å. The powder sample was housed in a Lindeman capillary tube with an inner diameter of 0.1 mm and rotated continuously during measurement to diminish the effect of preferred orientation. For above 800 K, we also utilized a $SiO_2$ capillary tube with an inner diameter of 0.2 mm. The ND and SXRD data collected at the same temperatures were fitted simultaneously by the Rietveld[52] method with the FullProf suite[53], otherwise they were fitted separately.

Optical SHG was measured for $Sr_3Sn_2O_7$ ($x$ = 0) in reflection geometry using a regeneratively amplified mode-locked Ti:sapphire laser (800 nm wavelength, 80 fs pulse duration, 1 kHz repetition rate). Temperature-dependent data were recorded in heating and cooling cycle between 300 and 460 K using a home-built heater. Differential scanning calorimetry (DSC) was also recorded for $x$ = 0 sample from room temperature to 700 K by using Rigaku Thermo Plus DSC 8270 at a heating rate of 10 K/min.

$^{119}$Sn Mössbauer spectroscopy was performed at room temperature for $(Sr_{1-x}Ca_x)_3Sn_2O_7$ ($x$ = 0, 0.1, and 0.2) in a transmission geometry using a $Ca^{119m}SnO_3$ γ-ray source. The source velocity and isomer shift were calibrated by α-Fe and $CaSnO_3$, respectively. The spectra were analyzed by least-squares fitting using Lorentzian functions.

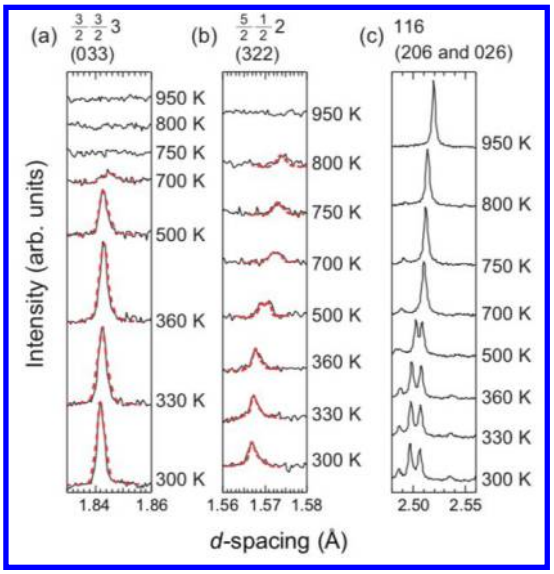
**First-principles calculations** We carried out DFT calculations for $Sr_3Sn_2O_7$ by using the projector augmented-wave (PAW) method[54,55] and PBEsol functional[56–58] as implemented in the VASP code[59–62]. We employed PAW datasets with radial cutoffs of 2.1, 1.6, and 0.8 Å for Sr, Sn, and O, respectively. Plane wave cutoff energy of 550 and 700 eV was utilized for structural optimization. We used cutoff energy of 400 eV otherwise. The following states were regarded as valence states: Sr 4s, 4p, and 5s; Sn 4d, 5s, and 5p; O 2$s$ and 2$p$. Lattice constants and fractional coordinates were optimized until the residual stress and forces converged down to 0.01 GPa and 1 meV/ Å, respectively.

Phonon frequencies and eigenvectors were calculated utilizing a frozen-phonon method as implemented in the PHONOPY code[63]. The phonon dispersion curves were drawn for a standard primitive cell[64,65] along a $q$-space path based on crystallography[66]. Our systematic stable structure exploration was conducted in a previously reported way[37,67–70]. Frequencies of the Brillouin zone-center phonon modes were calculated for a $\sqrt{2} \times \sqrt{2} \times 1$ supercell of the tetragonal conventional cell (space group: $I4/mmm$) of aristotype phase with a 4 × 4 × 1 $k$-point mesh. We note that zone-boundary phonon modes at the X and M points for an $I4/mmm$ primitive cell are included in the zone-center phonon modes for the supercell via band folding. When imaginary frequency phonon modes were found, we distorted the parent $I4/mmm$ aristotype structure according to the eigenvectors of the unstable modes, optimized the structural parameters of the lower-symmetry structures, and calculated the phonon frequencies to see if there is any phonon instability. This process was iterated unless the obtained structure was found to be dynamically stable. The cell metric was fixed during the stable structure exploration.

For energy surface calculations, structural distortions were decomposed into symmetry-adapted modes of the parent $I4/mmm$ phase using the AMPLIMODES[71] tool available at the Bilbao Crystallographic Server. The mode amplitude is defined as a square root of the sum of squared displacement vectors. The distortion patterns were visualized by the VESTA code[72].

## 3. RESULTS

**Room-temperature structure of $Sr_3Sn_2O_7$** The room-temperature structure of $Sr_3Sn_2O_7$ was previously reported by laboratory XRD and dark-field transmission electron microscopy[36]. We revisit the crystal structure at 300 K by using high-resolution ND, which provides much more accurate oxygen parameters than those obtained from XRD. Although the main reflections of the ND pattern at 300 K can be indexed with the tetragonal $I4/mmm$ aristotype structure, additional $h$+1/2 $k$+1/2 $l$ superlattice reflections (e.g., 3/2 3/2 3 reflection and 5/2 1/2 2 reflection in Figure 2a and 2b) were observed, together with the splitting of basic $hhl$ reflections (e.g., basic 116 reflection in Figure 2c). The superlattice reflections and reflection splittings are also found in the SXRD pattern at 300 K. These features indicate the symmetry-lowering from tetragonal to orthorhombic with an enlarged unit cell metric, $\sqrt{2}a_p \times \sqrt{2}a_p \times c_p$, where $a_p$ and $c_p$ are the pseudotetragonal lattice parameters. The larger cell was also reported in the previous works[36,73]. Note that no impurity phases were detected from either ND or SXRD data.






Accepted Manuscript

**Figure 2.** Temperature evolution of ND (a) 3/2 3/2 3 superlattice reflection, (b) 5/2 1/2 2 superlattice reflection, and (c) basic 116 reflection observed for $Sr_3Sn_2O_7$. Miller indices with respect to the $\sqrt{2}a_p \times \sqrt{2}a_p \times c_p$ unit cell are given in parentheses.

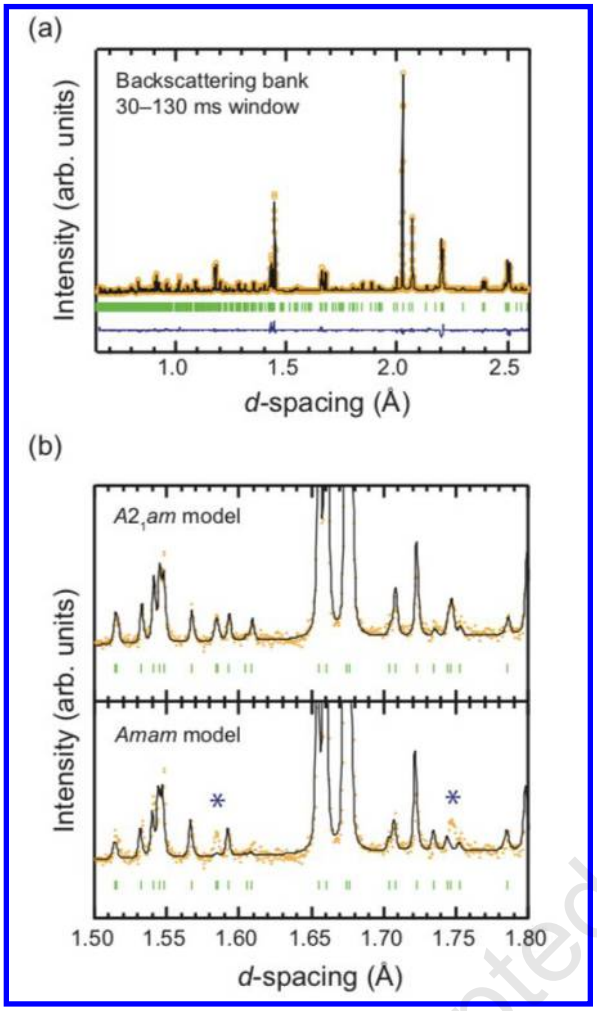



**Figure 3.** (a) Rietveld plot of ND data at 300 K for $Sr_3Sn_2O_7$ refined with a ferroelectric $A2_1am$ structural model. (b) An enlarged view of Rietveld plots of 300 K ND data for $Sr_3Sn_2O_7$ refined with $A2_1am$ and *Amam* structural models. Mismatches between the observed and calculated intensities are marked with asterisks. Orange circles and black and blue lines represent the observed, calculated and difference profiles, respectively. The green ticks show the position of Bragg reflections.

The observed reflection conditions in the orthorhombic setting are *hkl*: $k + l = 2n$, 0*kl*: $k + l = 2n$, *h*0*l*: $h, l = 2n$, *hk*0: $k = 2n$, *h*00: $h = 2n$, 0*k*0: $k = 2n$, and 00*l*: $l = 2n$ ($n$: integer). Noncentrosymmetric and polar $A2_1am$, and centrosymmetric and nonpolar *Amam* space groups have been derived from the reflection conditions and the compatibility with $n = 2$ RP structures. The structural model in $A2_1am$ symmetry involves two distinct OOT and OOR represented by $a^-a^-c^0$ and $a^0a^0c^+$, respectively, in Glazer notation[74], whereas the *Amam* structure only involves $a^-a^-c^0$-type OOT. These out-of-phase OOT and in-phase OOR modes transform as the irreducible representation (irrep) $X_3^-$, and $X_2^+$ of *I*4/*mmm*, respectively. The Rietveld refinement with a polar $A2_1am$ structural model against the ND pattern results in an excellent overall fit ($R_{wp}$ = 13.4%, see Figure 3a), while the *Amam* model cannot reproduce some observed peak intensities, for example, of *hk*0 ($h \neq 2n$, and $k = 2n$) reflections ($R_{wp}$ = 16.3%, see Figure 3b). The SXRD pattern is also fitted better with the $A2_1am$ model (Figure S1). Based on these results, we assign the crystal symmetry of $Sr_3Sn_2O_7$ at 300 K to the polar $A2_1am$.

This assignment is further verified by SHG measurement, which is a powerful technique to probe inversion symmetry breaking in piezoelectrics, pyroelectrics, and ferroelectrics[75]. A significant SHG signal is clearly observed over the temperature range of 300 K to about 400 K, indicating the absence of the inversion symmetry, i.e. the polar crystal structure with $A2_1am$ symmetry in this case. Our diffraction and optical experiments thus prove that $Sr_3Sn_2O_7$ crystallizes in polar $A2_1am$ symmetry at 300 K, in agreement with the previous work by Wang *et.al*[36] and our systematic stable structure exploration (see section S4).

We also checked the deviation in the stoichiometry. During combined Rietveld analysis against 300 K ND and SXRD data, the cation and anion site occupancies in the $A2_1am$ model were refined, but the refined occupancies were consistently within 1 or 2% of the expected values, Hence, the site occupancies were fixed at unity for all the sites in the final refinement. The structural parameters of the $A2_1am$ phase at 300 K obtained from joint refinements against the ND and SXRD data are listed in Table 1. We estimated the octahedral distortion in $Sr_3Sn_2O_7$ using the octahedral distortion parameter, $\Delta = 1/6\ \Sigma_i[(d_i - \langle d \rangle)/\langle d \rangle]^2$, where $d_i$ is the individual Sn–O bond length and $\langle d \rangle$ is the mean bond length in $SnO_6$ octahedra. We obtained $\Delta = 4.1 \times 10^{-5}$ for $SnO_6$ in $Sr_3Sn_2O_7$, which is smaller than that for $TiO_6$ ($\Delta = 1.6 \times 10^{-4}$) in $Ca_3Ti_2O_7$[32], where the SOJT effect of $Ti^{4+}(3d^0)$ ions leads to off-centering distortion of $TiO_6$ octahedra. Note that $Sn^{4+}$ ($4d^{10}$) is not SOJT-active, in contrast to $Sn^{2+}$ (which has a $5s^2$ lone pair of electrons).[6]

**Table 1. Structural parameters of $Sr_3Sn_2O_7$ at 300 K obtained from joint refinements with an $A2_1am$ model against ND and SXRD data.**

| Atom | site | *x* | *y* | *z* | $U_{iso}$ or $U_{eq}$ (Å$^2$) |
|---|---|---|---|---|---|
| O1 | 4a | 0.2505(19) | 0.7996(10) | 0 | 0.0110(12) |
| O2 | 8b | 0.2597(13) | 0.7091(6) | 0.19631(10) | 0.0059(7) |
| O3 | 8b | 0.5280(15) | 0.5295(8) | 0.08689(12) | 0.0038(8) |
| O4 | 8*b* | 0.4842(18) | 0.0143(10) | 0.10565(13) | 0.0142(8) |
| Sr1* | 4*a* | 0.2548(19) | 0.2491(10) | 0 | 0.0109(14) |
| Sr2* | 8*b* | 0.7374(10) | 0.7431(5) | 0.18846(6) | 0.0080(10) |
| Sn | 8*b* | 0.75† | 0.2492(6) | 0.09854(6) | 0.0018(2) |

Space group; $A2_1am$ (No. 36), $Z = 4$. The occupancy parameter is fixed to unity for all atoms. †Fixed to define an origin of the polar *a* axis. *Refined anisotropically. Cell parameters; $a$ = 5.70739(10) Å, $b$ = 5.73485(10) Å, and $c$ = 20.66861(5) Å. ND: $R_{wp}$ = 11.5%, $R_B$ = 7.85%, and $\chi^2$ = 4.89. SXRD: $R_{wp}$ = 12.7%, $R_B$ = 3.80%, and $\chi^2$ = 6.34.

Further, we performed $^{119}$Sn Mössbauer spectroscopy at room temperature to evaluate the valence state and local structure of tin ions. The result for $Sr_3Sn_2O_7$ is shown in

Not Corrected Manuscript

Figure 4. Stannous ($Sn^{2+}$) and stannic ($Sn^{4+}$) compounds are well known to differ widely in isomer shift on account of the difference in the oxidation state; the isomer shift values for $Sn^{2+}$ ions (2.3 ~ 4.5 mm/s) are always higher than those for $Sn^{4+}$ ions (–0.4 ~ 2.3 mm/s).[76] In the present case, a single broadened peak is observed with the isomer shift (approximately 0 mm/s) typical of $Sn^{4+}$-containing compounds. This result completely excludes the presence of $Sn^{2+}$ in our sample. The Mössbauer spectrum is well reproduced by an unresolved quadrupole doublet with an isomer shift of 0.01 mm/s and a quadrupole splitting of 0.33 mm/s. The small value of quadrupole splitting indicates highly symmetrical octahedral coordination for $Sn^{4+}$ with a small electric field gradient, and it is consistent with the small distortion of $SnO_6$ octahedra as demonstrated by the aforementioned structural analysis.

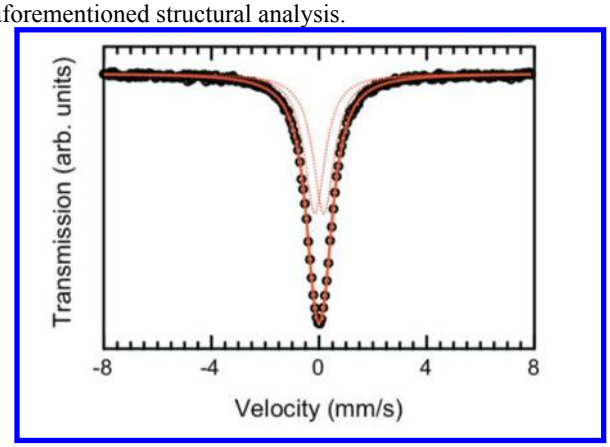



**Figure 4.** $^{119}$Sn Mössbauer spectrum at room temperature for $Sr_3Sn_2O_7$. The black circles and red solid line represent the experimental data and calculated curve, respectively. The red dotted curves depict a doublet component arising due to quadrupole splitting.

**Temperature-induced phase transitions of $Sr_3Sn_2O_7$** The SHG intensity of $Sr_3Sn_2O_7$ displayed in Figure 5a decreases with increasing temperature and drops to zero at 420 K, which indicates a phase transition from the noncentrosymmetric and polar $A2_1am$ phase to centrosymmetric and nonpolar one. Notably, SHG intensity on cooling behaves differently from that on heating; a substantial hysteresis (~10 K) was clearly

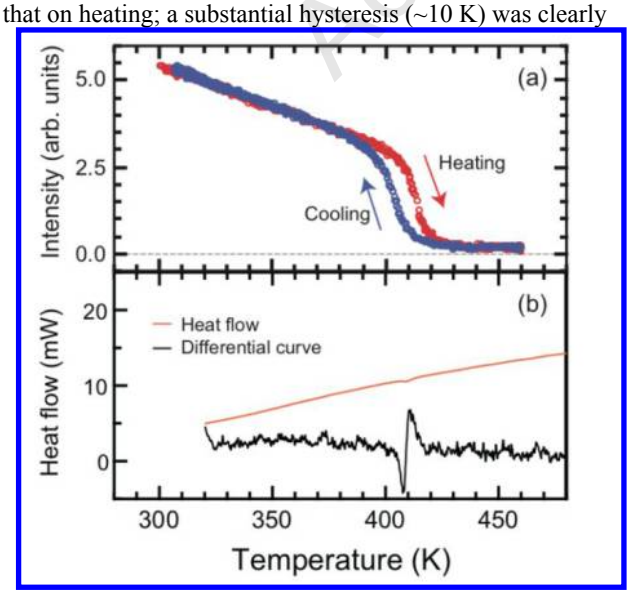



**Figure 5.** (a) Temperature dependence of SHG intensity of $Sr_3Sn_2O_7$ on heating (red) and cooling (blue). (b) DSC curve of $Sr_3Sn_2O_7$ on heating with the differential curve.

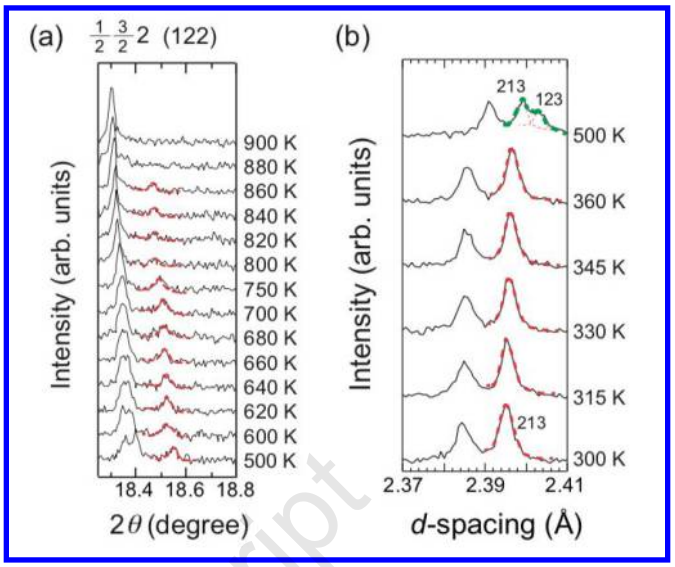



**Figure 6.** (a) Temperature evolution of SXRD 1/2 3/2 2 superlattice reflection observed for $Sr_3Sn_2O_7$ ($\lambda$ = 0.800484 Å). Miller indices with respect to the $\sqrt{2}a_p \times \sqrt{2}a_p \times c_p$ unit cell are given in parentheses. (b) Enlarged view of the temperature-variable ND pattern for $Sr_3Sn_2O_7$, highlighting an additional 123 reflection, which is indexed by the $\sqrt{2}a_p \times \sqrt{2}a_p \times c_p$ unit cell.

observed between heating and cooling curves. The DSC curve on heating (Figure 5b) shows an endothermic peak at 410 K, where the SHG intensity presents a hysteresis. These features suggest that $Sr_3Sn_2O_7$ undergoes a first-order ferroelectric-to-paraelectric transition at around $T_C$ = 410 K, in contrast to the previous report, where temperature-dependent resistivity data suggested that $T_C$ is beyond 1053 K[36].

To examine the appropriate crystal symmetry of the centrosymmetric phase, we here utilized ND and SXRD patterns collected at 500 K, a temperature slightly above $T_C$. At this temperature, the enlarged orthorhombic $\sqrt{2}a_p \times \sqrt{2}a_p \times c_p$ unit cell remains unchanged as confirmed by the superlattice reflection and the peak splitting (Figures 2a–c and 6a). A detailed inspection of the ND pattern shown in Figure 6b reveals some additional Bragg reflections upon heating to 500 K. As an example, the 123 reflection appears in the $d$-range of 2.39–2.41 Å, which is forbidden under the integral reflection condition of $A$-face centered lattices ($hkl$: $k + l = 2n$). The appearance of additional reflections signifies that the Bravais lattice type changes from $oA$ (orthorhombic $A$-centered lattice) to $oP$ (orthorhombic primitive lattice). Taking into account the lattice type, $oP$, extinction rules derived from Figure 2a ($0kl$: $k + l = 2n$ or nothing) and assuming the compatibility with $n$ = 2 RP structures[77], the plausible space groups are $Pnam$, $Pnab$, and $Pnnm$. Under these symmetries, rotational/tilting distortions represented by $a^-a^-c^+/a^-a^-(c^+)$, $a^-a^-c^-$ and $a^-b^-c^0$ are allowed, respectively. The $a^-a^-c^+/a^-a^-(c^+)$-type distortion describes the cooperative structural distortion, where the OORs in each perovskite layer are in-phase, but the direction of the rotation inverts between adjacent layers[78]. Owing to the high sensitivity of ND to

Accepted Manuscript

oxygen positions and thus rotational/tilting distortion patterns, we can determine a possible space group through Rietveld analysis. A structural model refined in *Pnab* symmetry provides a best fit to the ND pattern (Figure 7a) with a small agreement factor ($R_{wp}$ = 13.3%). The agreement factors for the *Pnam* and *Pnnm* models are worse ($R_{wp}$ = 15.7% and 16.6%, respectively), and the fitting curves for these two models more poorly capture the observed intensity as shown in Figure 7b. The Rietveld refinement with the *Pnab* model against the 500 K SXRD pattern also converges successfully (Figure. S2). These analyses clearly support the assignment of the orthorhombic *Pnab* structure to the paraelectric phase over the *Pnam* and *Pnnm* structures. The structural parameters of the *Pnab* phase at 500 K obtained from joint refinements against the ND and SXRD data are summarized in Table 2.

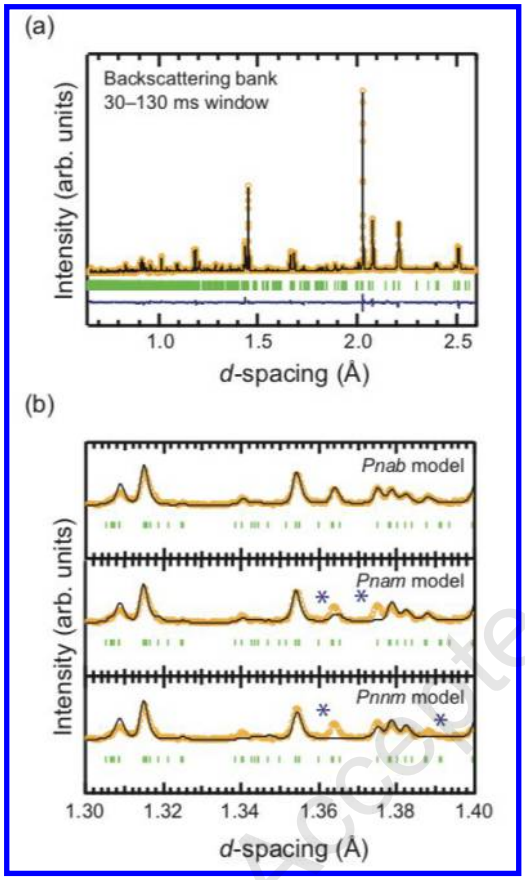



**Figure 7.** (a) Rietveld plot of ND data at 500 K for $Sr_3Sn_2O_7$ refined with a *Pnab* structural model. (b) An enlarged view of Rietveld plots of 500 K ND data for $Sr_3Sn_2O_7$ refined with *Pnab*, *Pnam*, and *Pnnm* structural models. Mismatches between the observed and calculated intensities are marked with asterisks. Orange circles and black and blue lines represent the observed, calculated and difference profiles, respectively. The green ticks show the position of Bragg reflections.

The distortion pattern in the paraelectric *Pnab* phase, $a^-a^-c^-$, is a combination of $a^-a^-c^0$-type OOT (irrep $X_3^-$) and $a^0a^0c^-$-type OOR (irrep $X_1^-$). Although out-of-phase OOT occurs in both the ferroelectric $A2_1am$ and paraelectric *Pnab* phases, there is a marked change in the sense of OOR across the ferroelectric-to-paraelectric transition; an in-phase OOR in the $A2_1am$ phase, corresponding to an $X_2^+$ mode ($a^0a^0c^+$), disappears, and out-of-phase $X_1^-$ mode ($a^0a^0c^-$) condenses in *Pnab* phase. There are no pathways along which the $a^0a^0c^+$-type OOR transforms directly and continuously to the out-of-phase OOR represented by $a^0a^0c^-$. Therefore, such a structural transformation should occur discontinuously; that is, the ferroelectric- to-paraelectric transition will be of first order. The first-order character of the ferroelectric transition is experimentally confirmed by temperature-variable SXRD data, as described in Section 4, which show that the $A2_1am$ and *Pnab* phases coexist with a substantial hysteresis on heating and cooling across the phase transition ($T_C$ ~ 410 K). The temperature evolution of the lattice parameters (*a*, *b*, and *c*) displays an obvious discontinuity around $T_C$ (Figure S6), validating the first-order nature of the ferroelectric transition.

**Table 2. Structural parameters of $Sr_3Sn_2O_7$ at 500 K obtained from joint refinements with a *Pnab* model against ND and SXRD data.**

| Atom | site | *x* | *y* | *z* | $U_{iso}$ or $U_{eq}$ (Å$^2$) |
|---|---|---|---|---|---|
| O1* | 4*a* | 0.75 | 0.7116(15) | 0 | 0.021(4) |
| O2 | 8*b* | 0.9813(14) | 0.0205(12) | 0.91081(14) | 0.0119(13) |
| O3* | 8*b* | 0.753(3) | 0.7780(11) | 0.80352(13) | 0.017(3) |
| O4 | 8*b* | 0.0293(14) | 0.0274(13) | 0.60290(17) | 0.0155(14) |
| Sr1* | 4*a* | 0.75 | 0.2500(12) | 0 | 0.0147(17) |
| Sr2* | 8*b* | 0.7553(12) | 0.2427(7) | 0.81159(7) | 0.0137(12) |
| Sn | 8*b* | 0.7503(11) | 0.7493(7) | 0.9016(7) | 0.0035(2) |

Space group; *Pnab* (No. 60), *Z* = 4. The occupancy parameter is fixed to unity for all atoms. *Refined anisotropically. Cell parameters; *a* = 5.71718(10) Å, *b* = 5.73526(10) Å, and *c* = 20.74162(7) Å. ND: $R_{wp}$ = 13.3%, $R_B$ = 7.59%, and $\chi^2$ = 5.44. SXRD: $R_{wp}$ = 13.7%, $R_B$ = 3.88%, and $\chi^2$ = 6.87.

Next, we identify the structural phase transitions at temperatures higher than $T_C$ (~ 410 K). The 033 reflection gets weaker and completely disappears at 750 K (Figure 2a), although other reflections (e.g. the 322 reflection), indicative of the cell doubling, are still visible (Figure 2b). The 033 reflection represents an example of 0*kl* ($k + l = 2n$) reflections that result from a condensation of $X_3^-$ mode, and hence, the disappearance of 033 reflection indicates the loss of $a^-a^-c^0$-type OOT in the *Pnab* phase. An $n$ = 2 RP structure involving only $a^0a^0c^-$-type OOR adopts a space group *Acaa*. Indeed, the structural model in orthorhombic *Acaa* symmetry captures the ND pattern at 750 K well (Figure S3). Since the orthorhombic splitting apparently disappears at 750 K (Figure 2c), we also carried out comparative refinements using tetragonal hettotype structures ($P4_2/mnm$ and $P4_2/mcm$); however, these tetragonal models are ruled out by their poor fits to the collected ND pattern (Figure S4). Thus, the lattice behavior shown in Figure 2c is attributed to a pseudotetragonal symmetry of the orthorhombic *Acaa* phase.

Finally, we identify the structural phase transition from *Acaa* to $I4/mmm$ structure through the temperature-variable ND and SXRD data. For ND data, all the superlattice reflections (e.g. the 322 reflection in Figure 2b) disappear at 950 K, where the sample adopts the tetragonal $I4/mmm$ aristotype structure. The SXRD data with a fine-temperature interval allows us to determine the phase-transition temperature. As shown in Figure 6a, the SXRD superlattice

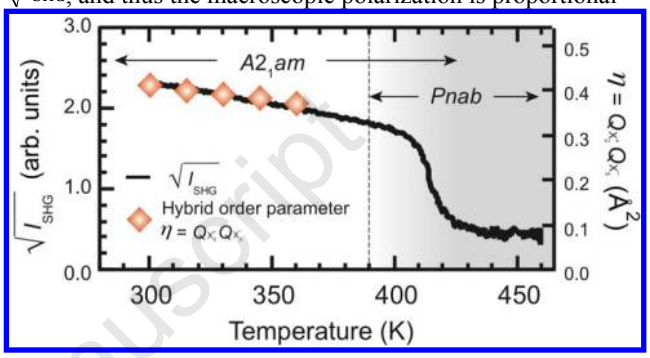
Accepted Manuscript

122 reflection disappears at 880 K, indicating the structural phase transition to the aristotype phase.

Our diffraction studies coupled with optical SHG measurements unveil the sequence of structural phase transitions of $n$ = 2 RP $Sr_3Sn_2O_7$; the ferroelectric-to-paraelectric transition of $Sr_3Sn_2O_7$ is observed for the first time. The phase transitions connecting ferroelectric $A2_1am$ phase to non-distorted paraelectric $I4/mmm$ phase proceed through the following sequence: $A2_1am$ ($a^-a^-c^+$) → $Pnab$ ($a^-a^-c^-$) → $Acaa$ ($a^0a^0c^-$) → $I4/mmm$ ($a^0a^0c^0$). The ferroelectric ($A2_1am$)-to-paraelectric ($Pnab$) transition involves an unusual change in the sense of OOR while the OOT remains unchanged. On heating above $T_C$, the $a^-a^-c^0$-type OOT disappears in the $Pnab$ → $Acaa$ transition, and then the $a^0a^0c^-$-type OOR finally vanishes, resulting in the $I4/mmm$ aristotype. The lattice parameters evolve continuously across the two structural phase transitions above $T_C$ (Figure S6). Indeed, the two pairs of space groups, $Pnab$–$Acaa$ and $Acaa$–$I4/mmm$, are in group-subgroup relationships, and the $Pnab$ → $Acaa$ and $Acaa$ → $I4/mmm$ transitions are allowed to be second-order, i.e., continuous. The phase diagram and crystal structures of the observed four phases are summarized in Figure 1.

## 4. DISCUSSION

**Verification of the hybrid improper ferroelectricity in $Sr_3Sn_2O_7$** Hybrid improper ferroelectrics are phenomenologically characterized by the presence of the specific term, $PQ_1Q_2$, in their free-energy series, where $P$ is the macroscopic polarization and $Q_1$ and $Q_2$ are the mode amplitudes of two distinct nonpolar distortions[11]. Given the form of the trilinear term, $PQ_{X_3^-}Q_{X_2^+}$, of $n$ = 2 RP hybrid improper ferroelectrics, the polarization would be proportional to a hybrid order parameter, $\eta = Q_{X_3^-}Q_{X_2^+}$, where $Q_{X_3^-}$ and $Q_{X_2^+}$ are the amplitude of $X_3^-$ and $X_2^+$ modes, respectively. To verify experimentally this behavior in the polar $A2_1am$ phase of $Sr_3Sn_2O_7$, we compare the temperature dependence of the SHG intensity ($I_{SHG}$) and $\eta$ in the temperature range of 300 to 360 K. From the relationship between nonlinear optical tensor coefficients and $P$, the temperature dependence of the polarization can be estimated by using that of the SHG intensity: $P \propto \sqrt{I_{SHG}}$[69,75]. The $\eta$ values are obtained through a symmetry-mode analysis of the refined structures with the aid of AMPLIMODES software[71]. Figure 8 illustrates that the temperature dependence of $\eta$ has a similar trend to that of $\sqrt{I_{SHG}}$, and thus the macroscopic polarization is proportional



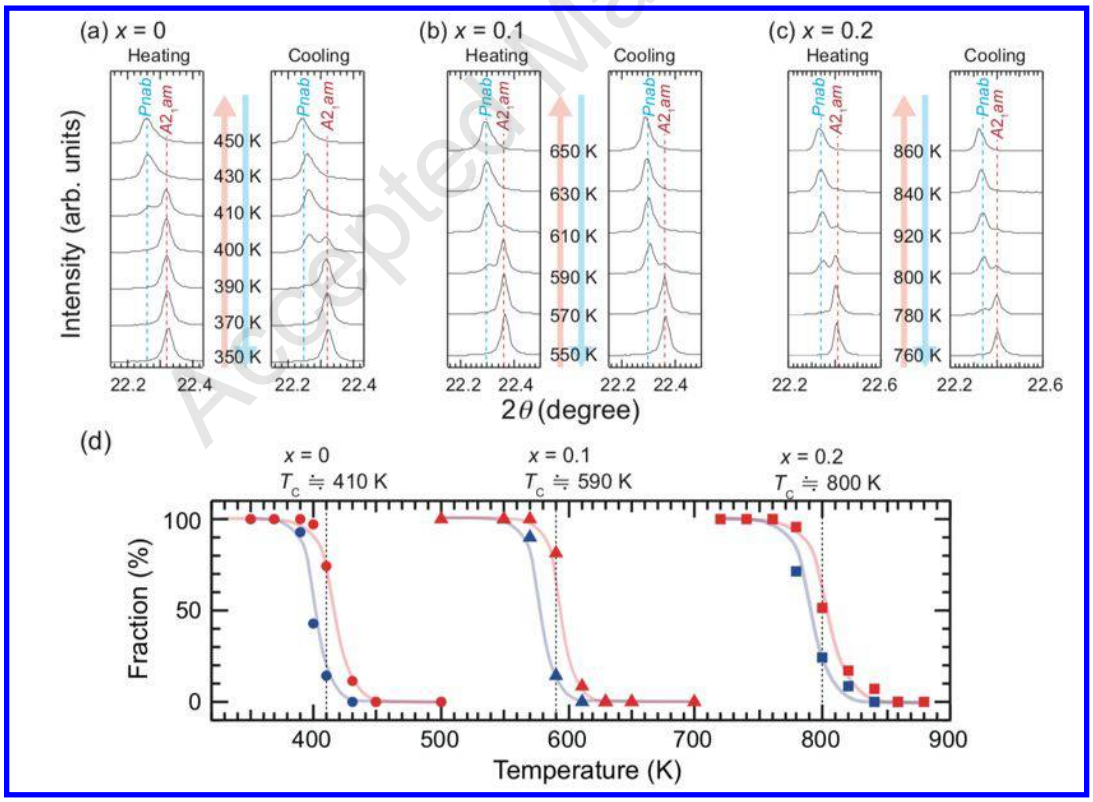




**Figure 9.** (a)–(c) Temperature dependence of SXRD ($\lambda$ = 0.800484 Å) 0010 reflection of $(Sr_{1-x}Ca_x)_3Sn_2O_7$ ($x$ = 0, 0.1, and 0.2) on heating and cooling across the ferroelectric-to-paraelectric transition between $A2_1am$ and $Pnab$ phases. (d) Temperature evolution of the weight fraction of ferroelectric $A2_1am$ phase of $(Sr_{1-x}Ca_x)_3Sn_2O_7$ ($x$ = 0, 0.1, and 0.2) on heating (red) and cooling (blue). Circles, triangles, and squares represent the calculated values from multiphase Rietveld refinements against SXRD data for $x$ = 0, 0.1, and 0.2 samples, respectively, and the solid lines are given for eye guide. The vertical dashed line for each sample indicates the center of hysteresis, corresponding to the ferroelectric-to-paraelectric transition temperature ($T_C$); $T_C$ ~ 410 K for $x$ = 0, $T_C$ ~ 590 K for $x$ = 0.1, and $T_C$ ~ 800 K for $x$ = 0.2.

Accepted Manuscript

**Figure 8.** Temperature dependence of the square root of SHG intensity, $\sqrt{I_{SHG}}$, and the hybrid order parameter, $\eta = Q_{X_3^-} Q_{X_2^+}$, for $Sr_3Sn_2O_7$.

to $\eta$. This result strongly supports the existence of an anharmonic coupling between the OOR/OOT modes and the polar displacement. Our DFT calculations (see Section S4) also revealed that the OOR and OOT serve as the primary order parameters inducing the $A2_1am$ polar structure and that the polar displacement is just a by-product of the rotational/tilting distortions. Our experimental and first-principles results prove the chemical intuition that $Sr_3Sn_2O_7$ is an ideal hybrid improper ferroelectric, for which a proper mechanism driven by the SOJT effect plays no role at all in stabilizing the ferroelectric phase.

**Universal relationship of Curie temperatures and tolerance factors** So far, we have demonstrated that $n = 2$ RP $Sr_3Sn_2O_7$ is a hybrid improper ferroelectric with $T_C = 410$ K, where the polar displacements are induced by a combination of OOR and OOT. Since the OOR and OOT arise from size mismatch of *A*- and *B*-site cations, it is interesting to examine the effect of changing the *A*-site-cation size on rotational/tilting distortions, and hence on ferroelectric transition. We additionally prepared Ca-substituted series, $(Sr_{1-x}Ca_x)_3Sn_2O_7$ ($x$ = 0.1 and 0.2), and investigated their thermally-induced phase-transition behavior including ferroelectric-to-paraelectric transitions. The characterization by ND, SXRD, and $^{119}$Sn Mössbauer spectroscopy revealed that Ca-substituted series ($x$ = 0.1 and 0.2) also adopt the ferroelectric $A2_1am$ structure at 300 K (Figures S12 and S14), with the Sn ions being present in a tetravalent state (Figure S11). The lattice parameters ($a$, $b$, and $c$) decrease with the substitution of a smaller cation (i.e., $Ca^{2+}$) for $Sr^{2+}$ on the *A*-site.

In order to probe the ferroelectric transition behavior, we utilize temperature-dependent SXRD patterns on heating and cooling. Figure 9a–c displays SXRD 0010 reflections of $(Sr_{1-x}Ca_x)_3Sn_2O_7$ ($x$ = 0, 0.1, and 0.2) as a function of temperature. A first-order phase transition is observed around 410 K ($x$ = 0, Figure 9a), 590 K ($x$ = 0.1, Figure 9b) and 800 K ($x$ = 0.2, Figure 9c); one can see phase coexistence and hysteresis on heating and cooling. Similar to the case of $Sr_3Sn_2O_7$ ($x$ = 0), the SXRD patterns for $x$ = 0.1 and 0.2 samples at temperatures above the phase transitions are fitted well based on structural models in *Pnab* symmetry (Figures S13 and S15). The weight fractions of the ferroelectric $A2_1am$ phase for $x$ = 0, 0.1, and 0.2 samples are plotted in Figure 9d as a function of temperature. We define $T_C$ as the center of the thermal hysteresis curve. We see that for $x$ = 0 the hysteresis loop of the ferroelectric phase fraction in the vicinity of $T_C$ follows completely that of the SHG intensity as depicted in Figure 5a (see also Figure S16). As expected from the geometric origin of the hybrid improper ferroelectricity, the introduction of a smaller *A*-site cation, i.e. the partial substitution of $Ca^{2+}$ for $Sr^{2+}$ ($x$ = 0.1 and 0.2), enhances the magnitudes of OOR and OOT, resulting in higher $T_C$s.

To quantitatively describe the rotational/tilting distortion preference, we introduce Goldschmidt tolerance factor, $t$, which gives a simple measure of the size mismatch of constituent cations. Shannon's six-coordinate ionic radii[79] are used here. A non-distorted structure forms with $t \sim 1.0$, whereas for smaller $t$ values ($0.8 < t < 1.0$), the *A*-site cation is too small for its site resulting in a low-symmetry structure with rotated and/or tilted $BO_6$ octahedra. Figure 10 plots the $T_C$s of $(Sr_{1-x}Ca_x)_3Sn_2O_7$ ($x$ = 0, 0.1, and 0.2) system as a

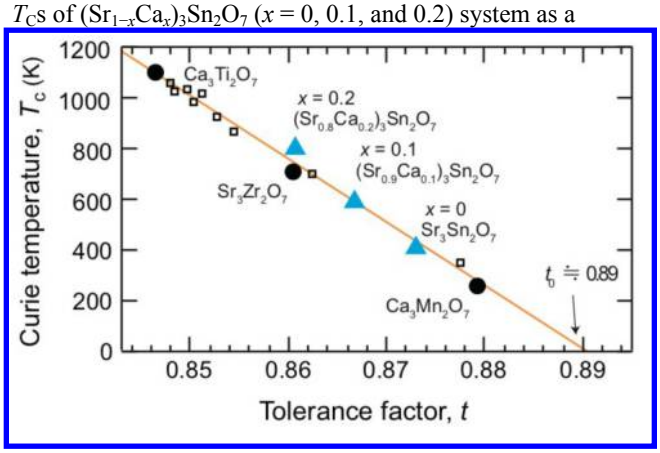



**Figure 10.** Curie temperatures ($T_C$) of $n$ = 2 RP ferroelectrics against the tolerance factor ($t$) of their perovskite unit. The result of linear fitting is depicted by an orange line with the critical $t$ value, $t_0$. Blue triangles represent the data for $(Sr_{1-x}Ca_x)_3Sn_2O_7$ ($x$ = 0, 0.1, and 0.2) obtained in this work. The black circles show the data previously reported for $Ca_3Ti_2O_7$,[32] $Sr_3Zr_2O_7$,[37] and $Ca_3Mn_2O_7$.[40] The squares indicate the reported data for solid-solution systems, $(Ca,Sr)_3Ti_2O_7$[34] and $Ca_3(Ti,Mn)_2O_7$.[32,35]

function of $t$. $T_C$ is found to monotonically increase with decreasing $t$. Because of the ubiquity of $t$ in characterizing perovskite units, we can extend the compositional range to other $n$ = 2 RP ferroelectrics. In addition to $(Sr,Ca)_3Sn_2O_7$, we consider twelve known RP compounds, i.e., $Ca_3Ti_2O_7$[32], $Ca_3Mn_2O_7$[40], $Sr_3Zr_2O_7$[37], $(Ca,Sr)_3Ti_2O_7$[34], and $Ca_3(Ti,Mn)_2O_7$[32,35]. In the suite of fifteen different $A_3B_2O_7$ ferroelectrics, $T_C$s range from below room temperature (~ 280 K) to about 1100 K. We find a linear relationship between the $T_C$ and $t$ (Figure 10). Given the chemical diversity of $n$ = 2 RP phases, the strong correlation between $T_C$ and $t$ is remarkable. From a linear extrapolation of this relation, one can see that an $n$ = 2 RP compound with $t$ = 0.89 has $T_C$ = 0 K. In other words, $t$ = 0.89 is an upper limit, $t_0$, for an $n$ = 2 RP compound to crystallize in a ferroelectric $A2_1am$ structure. Recent theoretical calculations also revealed that the ferroelectric $A2_1am$ structure is destabilized when $t > 0.89$; $Ca_3Ge_2O_7$ ($t$ = 0.879) has the $A2_1am$ ground state, whereas $Sr_3Tc_2O_7$ ($t$ = 0.892) exhibits a tilted but nonpolar $P4_2/mnm$ ground structure[51]. Although local structural disorder exists in solid solutions of $A_3B_2O_7$ ferroelectric, it has little effect on the $T_C$, and hence, the average $t$ values strongly correlate with the $T_C$. The minor effect of local structural disorder on $T_C$ was also observed for ferroelectric $Pb(Zr_{1-x}Ti_x)O_3$ solid solutions, where the $T_C$ is a smooth and monotonic function of $x$.[80] The universal relationship shown in Figure 10 proves a controllability of $T_C$ over a wide temperature range with the geometric effect (ionic-size mismatch) in hybrid improper ferroelectrics. The close relationship between $T_C$ and $t$ provides a useful guide for designing materials with the desired properties for a given application and also for predicting $T_C$s of as-yet-unsynthesized materials.

Previously, Abrahams *et al.*[81] have reported a simple relationship between $T_C$ and polarization ($P$), $T_C \propto P^2$, for

Accepted Manuscript

proper ferroelectrics such as $BaTiO_3$. According to this report, we also explore the relationships between $P$ and $T_C$ in hybrid improper ferroelectrics. A recent theoretical study on hybrid improper ferroelectric $A_3B_2O_7$ compounds ($A$ = Mg, Ca, and Sr, $B$ = Zr, Sn, and Ge) revealed that the $P$ values calculated by using Born effective charge are a smooth and monotonic function of $t$ (Figure S17).[15] One can find a linear relationship between $P$ and $t$. From this result (Figure S17) and the linear relationship between $T_C$ and $t$ (Figure 10), we expect $T_C \propto P$ for hybrid improper ferroelectrics, in contrast to the case of proper ferroelectrics. For $Ca_3Ti_2O_7$[32], $Ca_3Mn_2O_7$[33], $Sr_3Zr_2O_7$[37], and $Sr_3Sn_2O_7$[36] ceramics, we observe that the $T_C$s tend to correlate linearly with the experimental $P$ values obtained through ferroelectric hysteresis measurements (Figure S18). It should be noted that the $P$ values were measured for polycrystalline samples. The polarization measurements for single crystals will provide more reliable verification of the relationship between $T_C$ and $P$.

Interestingly, all the $A_3B_2O_7$ compounds listed in Figure 10 exhibit the first-order nature of the ferroelectric transition. For $Ca_3Ti_2O_7$ and $Ca_3(Ti,Mn)_2O_7$, the first-order transition between the ferroelectric $A2_1am$ ($a^-a^-c^+$) and the non-distorted $I4/mmm$ ($a^0a^0c^0$) phases has been suggested on the basis of the DSC and SXRD results[32]. As for the other compounds, the first-order ferroelectric transition is characterized by a competition between the ferroelectric $A2_1am$ phase and a distorted nonpolar polymorph. In the case of $Sr_3Zr_2O_7$, the competing metastable polymorph to the $A2_1am$ phase has $Pnab$ symmetry involving $a^-a^-c^-$-type distortion[37]. The $Pnab$ phase is stabilized by a hybrid improper *antiferroelectric* mechanism whereby an antipolar mode arises from a trilinear coupling to the OOR and OOT modes (see section S4); the induced antipolar mode leads to a complete cancellation of the layer polarization, providing no net macroscopic polarization (Figure 1a). Namely, there is a competition between hybrid improper ferroelectric and antiferroelectric mechanisms in $Sr_3Zr_2O_7$. This result corroborates the theoretical prediction[50,51] and shows the importance of understanding anharmonic interactions among lattice degrees of freedom. The present compounds, $(Sr,Ca)_3Sn_2O_7$, undergo the same ferroelectric transition as $Sr_3Zr_2O_7$ ($A2_1am$ to $Pnab$), again highlighting the interplay between the anharmonic interactions active in layered oxides. For $(Ca,Sr)_3Mn_2O_7$ system[39,40] with relatively larger $t$ values, a nonpolar polymorph with $Acaa$ symmetry involving only $a^0a^0c^-$-type OOR is observed as the competing metastable phase to the $A2_1am$ phase. The $Acaa$ phase exhibits a uniaxial negative thermal expansion along $c$ axis[82]. As shown in Figure S6, we also observe a similar phenomenon, i.e., uniaxial negative thermal expansion along $c$ axis, in the intermediate $Acaa$ phase for $Sr_3Sn_2O_7$. The two intermediate $Pnab$ and $Acaa$ phases, as well as the ground-state ferroelectric $A2_1am$ phase, have novel physical properties that stem from their rotational/tilting distortions. Hence, it would be interesting to stabilize the two intermediate phases at room temperature by chemical tuning according to the $T_C$ vs $t$ relationship established in this work.

## 5. SUMMARY

In conclusion, we demonstrate that $n$ = 2 RP $Sr_3Sn_2O_7$ is an ideal hybrid improper ferroelectric, where the SOJT effect plays no role at all in driving ferroelectric transition. Instead, the nonpolar OOR and OOT distortions trilinearly couple to create the ferroelectric polarization as a by-product. In contrast to the previous report[36], we observe a first-order ferroelectric-to-paraelectric transition in $Sr_3Sn_2O_7$ ($T_C$ = 410 K). We also show that the isovalent substitution of $Ca^{2+}$ for $Sr^{2+}$, which leads to a decrease in $t$, increases $T_C$ up to 800 K. Remarkably, we find a linear relationship between $T_C$ and $t$ across the suite of fifteen $A_3B_2O_7$ compounds consisting of RP ferroelectrics reported here and those reported previously. This relationship provides a predictive guideline for estimating $T_C$ of a given material, which would complement the design approach based on group theory and first principles. Further, the findings open routes to the possible use of hybrid improper ferroelectrics in technological applications: for example, pyroelectric energy harvesting[83–85], where the tunability of $T_C$ is advantageous for achieving a large electrothermal coupling factor.

## ASSOCIATED CONTENT

### Supporting Information

The Supporting Information is available free of charge on the ACS Publications website at DOI:.

Additional ND and SXRD analyses, first-principles calculation results, and Mössbauer spectroscopy (PDF).

## AUTHOR INFORMATION


### Corresponding Author

*fujita.koji.5w@kyoto-u.ac.jp

### Present Addresses

¶ H.A.: Department of Applied Chemistry, Kyushu University, Motooka, Fukuoka 819-0395, Japan


## ACKNOWLEDGMENT

This work was supported by the JSPS KAKENHI (Grant Numbers JP16H04496, JP17H01320, JP18K8940, JP17K19172, JP18H01892), the Grant-in-Aid for JSPS Research Fellow (Grant Number JP17J07106), and the National Science Foundation Penn State Center for Nanoscale Science MRSEC grant number DMR-1420620. SXRD experiments were performed on BL02B2 at SPring-8 with the approval of JASRI (Proposal Nos. 2017B11423 and 2018A1391). Time-of-flight ND experiments on HRPD at the ISIS Pulsed Neutron and Muon Source were supported by beam time allocations from STFC (RB1620102 and RB1790074). The Mössbauer spectroscopic measurements were performed under the Nanotechnology Platform Program by MEXT, Japan.

## REFERENCES


(1) Scott, J. F. *Science* **2007**, *315*, 954–959.
(2) Cohen, R. E. *Nature* **1992**, *358*, 136–138.
(3) Hill, N. A. *J. Phys. Chem. B* **2000**, *104*, 6694–6709.
(4) Bersuker, I. B. *Phys. Rev. Lett.* **2012**, *108*, 137202.
(5) Rondinelli, J. M.; Eidelson, A. S.; Spaldin, N. A. *Phys. Rev. B* **2009**, *79*, 205119.
(6) Walsh, A.; Payne, D. J.; Egdell, R. G.; Watson, G. W. *Chem. Soc. Rev.* **2011**, *40*, 4455–4463.
(7) Koopmans, H. J. A.; Van De Velde; G. M. H.; Gellings, P. J. *Acta Cryst. Sect. C* **1983**, *39*, 1323–1325.
(8) Ahtee, A.; Ahtee M. *Acta Cryst. Sect. B*, **1976**, *32*, 3243–3246.
(9) Levin, I.; Amos, T. G.; Bell, S. M.; Farber, L.; Vanderah, T. A. Roth, R. S.; Toby, B. H. *J. Solid State Chem.* **2003**, *175*, 170–181.
(10) Sawaguchi, E. *J. Phys. Soc. Japan* **1953**, *8*, 615–629.
(11) Benedek, N. A.; Fennie, C. J. *Phys. Rev. Lett.* **2011**, *106*, 107204.

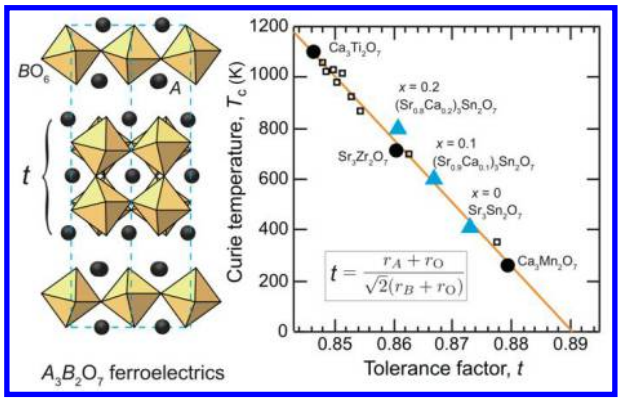

ACS Paragon Plus Environment Manuscript

(12) Benedek, N. A.; Mulder, A. T.; Fennie, C. J. *J. Solid State Chem.* **2012**, *195*, 11–20.
(13) Harris, A. B. *Phys. Rev. B* **2011**, *84*, 064116.
(14) Bousquet, E.; Dawber, M.; Stucki, N.; Lichtensteiger, C.; Hermet, P.; Gariglio, S.; Triscone, J.-M.; Ghosez, P. *Nature* **2008**, *452*, 732–736.
(15) Mulder, A. T.; Benedek, N. A.; Rondinelli, J. M.; Fennie, C. J. *Adv. Funct. Mater.* **2013**, *23*, 4810.
(16) Ruddlesden, S. N.; Popper, P. *Acta Crystallogr.* **1957**, *10*, 538–539.
(17) Benedek, N. A. *Inorg. Chem.* **2014**, *53*, 3769–3777.
(18) Benedek, N. A.; Rondinelli, J. M.; Djani, H.; Ghosez, P.; Lightfoot, P. *Dalt. Trans.* **2015**, 44, 10543–10558
(19) Young, J.; Stroppa, A.; Picozzi, S.; Rondinelli, J. M. *J. Phys. Condens. Matter* **2015**, *27* (28), 283202.
(20) Boström, H. L. B.; Senn, M. S.; Goodwin, A. L. *Nat. Commun.* **2018,** *9*, 2380.
(21) Karen, V. L.; Hellenbrandt, M. *Acta Crystallogr. Sect. A* **2002,** *58*, c367.
(22) Rondinelli, J. M.; Fennie, C. J. *Adv. Mater.* **2012**, *24*, 1961–1968.
(23) Young, J.; Rondinelli, J. M. *Chem. Mater.* **2013**, *25*, 4545–4550.
(24) An, M.; Zhang, H.-M.; Weng, Y.-K.; Zhang, Y.; Dong, S. *Front. Phys.* **2015**, *11*, 117501.
(25) Balachandran, P. V; Puggioni, D.; Rondinelli, J. M. *Inorg. Chem.* **2014**, *53*, 336–348.
(26) Young, J.; Stroppa, A.; Picozzi, S.; Rondinelli, J. M. *Dalt. Trans.* **2014**, *44*, 10644–10653.
(27) Zhao, H. J.; Ren, W.; Yang, Y.; Íñiguez, J.; Chen, X. M.; Bellaiche, L. *Nat. Commun.* **2014**, *5*, 4021.
(28) Balachandran, P. V.; Young, J.; Lookman, T.; Rondinelli, J. M. *Nat. Commun.* **2017**, *8*, 14282.
(29) Puggioni, D.; Rondinelli, J. M. *Nat. Commun.* **2014**, *5*, 3432.
(30) Sim, H.; Cheong, S. W.; Kim, B. G. *Phys. Rev. B* **2013**, *88*, 014101.
(31) Oh, Y. S.; Luo, X.; Huang, F.-T.; Wang, Y.; Cheong, S.-W. *Nat. Mater.* **2015**, *14*, 407–413.
(32) Liu, X. Q.; Wu, J. W.; Shi, X. X.; Zhao, H. J.; Zhou, H. Y.; Qiu, R. H.; Zhang, W. Q.; Chen, X. M. *Appl. Phys. Lett.* **2015**, *106*, 202903.
(33) Liu, M.; Zhang, Y.; Lin, L.-F.; Lin, L.; Yang, S.; Li, X.; Wang, Y.; Li, S.; Yan, Z.; Wang, X.; Li, X.-G.; Dong, S.;Liu, J.-M. *Appl. Phys. Lett.* **2018**, *113*, 022902.
(34) Li, G. J.; Liu, X. Q.; Lu, J. J.; Zhu, H. Y.; Chen, X. M.. *J. Appl. Phys.* **2018**, *123*, 014101.
(35) Gao, B.; Huang, F.-T.; Wang, Y.; Kim, J.-W.; Wang, L.; Lim, S.-J.; Cheong, S.-W. *Appl. Phys. Lett.* **2017**, *110*, 222906.
(36) Wang, Y.; Huang, F.-T.; Luo, X.; Gao, B.; Cheong, S.-W. *Adv. Mater.* **2016**, *29*, 1601288.
(37) Yoshida, S.; Fujita, K.; Akamatsu, H.; Hernandez, O.; Sen Gupta, A.; Brown, F. G.; Padmanabhan, H.; Gibbs, A. S.; Kuge, T.; Tsuji, R.; Murai, S.; Rondinelli, J. M.; Gopalan, V.; Tanaka, K. *Adv. Funct. Mater.* **2018**, *28*, 1801856.
(38) Li, X.; Yang, L.; Li, C. F.; Liu, M. F.; Fan, Z.; Xie, Y. L.; Lu, C. L.; Lin, L.; Yan, Z. B.; Zhang, Z.; Dai, J. Y.; Liu, J.-M.; Cheong, S.-W. *Appl. Phys. Lett.* **2017**, *110*, 042901.
(39) Senn, M. S.; Murray, C. A.; Luo, X.; Wang, L.; Huang, F.-T.; Cheong, S.-W.; Bombardi, A.; Ablitt, C.; Mostofi, A. A.; Bristowe, N. C. *J. Am. Chem. Soc.* **2016**, *138*, 5479–5482.
(40) Senn, M. S.; Bombardi, A.; Murray, C. A.; Vecchini, C.; Scherillo, A.; Luo, X.; Cheong, S. W. *Phys. Rev. Lett.* **2015**, *114*, 035701.
(41) Strayer, M. E.; Gupta, A. Sen; Akamatsu, H.; Lei, S.; Benedek, N. A.; Gopalan, V.; Mallouk, T. E. *Adv. Funct. Mater.* **2016**, *26*, 1930–1937.
(42) Dixon, C.; McNulty, J.; Knight, K.; Gibbs, A.; Lightfoot, P. *Crystals* **2017**, *7*, 135.
(43) Pitcher, M. J.; Mandal, P.; Dyer, M. S.; Alaria, J.; Borisov, P.; Niu, H.; Claridge, J. B.; Rosseinsky, M. *J. Science* **2015**, *347*, 420–424.
(44) Zhu, T.; Cohen, T.; Gibbs, A. S.; Zhang, W.; Halasyamani, P. S.; Hayward, M. A.; Benedek, N. A. *Chem. Mater.* **2017**, *29*, 9489–9497.
(45) Young, J.; Moon, E. J.; Mukherjee, D.; Stone, G.; Gopalan, V.; Alem, N.; May, S. J.; Rondinelli, J. M. *J. Am. Chem. Soc.* **2017**, *139*, 2833–2841.
(46) Retuerto, M.; Li, M. R.; Ignatov, A.; Croft, M.; Ramanujachary, K. V.; Chi, S.; Hodges, J. P.; Dachraoui, W.; Hadermann, J.; Tran, T. T.; Halasyamani, P. S.; Grams, C. P.; Hemberger, J.; Greenblatt, M. *Inorg. Chem.* **2013**, *52*, 12482–12491.
(47) Zhong, W.; Vanderbilt, D.; *Phys. Rev. Lett.* **1994**, *73*, 1861–1864.
(48) Paul, A.; Sun, J.; Perdew, J. P.; Waghmare, U. V. *Phys. Rev. B* **2017**, *95*, 054111.
(49) Nishimatsu, T.; Iwamoto, N; Kawazoe, Y.; Waghmare, U. V. *Phys. Rev. B* **2010**, *82*, 134106.
(50) Lu, X.-Z.; Rondinelli, J. M. *Nat. Mater.* **2016**, *15*, 951–955.
(51) Lu, X.-Z.; Rondinelli, J. M. *Adv. Funct. Mater.* **2016**, *27*, 1604312.
(52) Rietveld, H. M. *J. Appl. Crystallogr.* **1969**, *2*, 65–71.
(53) Rodríguez-Carvajal, J. *Phys. B Condens. Matter* **1993**, *192*, 55–69.
(54) Blöchl, P. E. *Phys. Rev. B* **1994**, *50*, 17953–17979.
(55) Kresse, G.; Joubert, D. *Phys. Rev. B* **1999**, *59*, 1758–1775.
(56) Perdew, J. P.; Burke, K.; Ernzerhof, M. *Phys. Rev. Lett.* **1996**, *77*, 3865–3868.
(57) Perdew, J. P.; Burke, K.; Ernzerhof, M. *Phys. Rev. Lett.* **1997**, *78*, 1396.
(58) Perdew, J. P.; Ruzsinszky, A.; Csonka, G. I.; Vydrov, O. A.; Scuseria, G. E.; Constantin, L. A.; Zhou, X.; Burke, K. *Phys. Rev. Lett.* **2008**, *100*, 136406.
(59) Kresse, G.; Hafner, J. *Phys. Rev. B* **1993**, *48*, 13115–13118.
(60) Kresse, G.; Hafner, J. *Phys. Rev. B* **1993**, *47*, 558–561.
(61) Kresse, G.; Furthmüller, J. *Comput. Mater. Sci.* **1996**, *6*, 15–50.
(62) Kresse, G.; Furthmüller, J. *Phys. Rev. B* **1996**, *54*, 11169–11186.
(63) Togo, A.; Tanaka, I. *Scr. Mater.* **2015**, *108*, 1–5.
(64) Hinuma, Y.; Togo, A.; Hayashi, H.; Tanaka, I. **2015**, arXiv:cond-mat/1506.01455. arXiv.org e-Print archive. http://arxiv.org/abs/1506.01455 (accessed Nov 30, 2017)
(65) Setyawan, W.; Curtarolo, S. *Comput. Mater. Sci.* **2010**, *49*, 299–312.
(66) Hinuma, Y.; Pizzi, G.; Kumagai, Y.; Oba, F.; Tanaka, I. *Comput. Mater. Sci.* **2017**, *128*, 140–184.
(67) Togo, A.; Tanaka, I. *Phys. Rev. B* **2013**, *87*, 184104.
(68) Akamatsu, H.; Fujita, K.; Kuge, T.; Sen Gupta, A.; Togo, A.; Lei, S.; Xue, F.; Stone, G.; Rondinelli, J. M.; Chen, L.-Q.; Tanaka, I.; Gopalan, V.; Tanaka, K. *Phys. Rev. Lett.* **2014**, *112*, 187602.
(69) Sen Gupta, A.; Akamatsu, H.; Strayer, M. E.; Lei, S.; Kuge, T.; Fujita, K.; dela Cruz, C.; Togo, A.; Tanaka, I.; Tanaka, K.; Mallouk, T. E.; Gopalan, V. *Adv. Electron. Mater.* **2016**, *2*, 1500196.
(70) Sen Gupta, A.; Akamatsu, H.; Brown, F. G.; Nguyen, M. A. T.; Strayer, M. E.; Lapidus, S.; Yoshida, S.; Fujita, K.; Tanaka, K.; Tanaka, I.; Mallouk, T. E.; Gopalan, V. *Chem. Mater.* **2017**, *29*, 656–665.
(71) Orobengoa, D.; Capillas, C.; Aroyo, M. I.; Perez-Mato, J. M. *J. Appl. Crystallogr.* **2009**, *42*, 820–833.
(72) Momma, K.; Izumi, F. *J. Appl. Crystallogr.* **2011**, *44*, 1272–1276.
(73) Green, M. A.; Prassides, K.; Day, P. ; Neumann, D. A.; *Int. J. Inorg. Mater.* **2000**, *2*, 35–41.
(74) Glazer, A. M. *Acta Crystallogr. Sect. B* **1972**, *28*, 3384–3392.
(75) Denev, S. A.; Lummen, T. T. A.; Barnes, E.; Kumar, A.; Gopalan, V. *J. Am. Ceram. Soc.* **2011**, *94*, 2699–2727.
(76) Greenwood, N. N.; Gibb, T. C. *Mössbauer Spectroscopy*; Chapman and Hall: London, U.K., 1971.
(77) Aleksandrov, S. K. *Crystallography Reports*. **1995,** *40*, 251–272.
(78) Zhang, Z.; Senn, M. S.; Hayward, M. A. *Chem. Mater.* **2016**, *28*, 8399–8406.
(79) Shannon, R. D. *Acta Crystallogr. Sect. A* **1976**, *32*, 751–767.
(80) Noheda, B; Cox, D. E.; Shirane, G.; Gonzalo, J. A.; Cross, L. E.; Park, S.-E. *Appl. Phys. Lett.* **1999**, 74, 2059–2061.

Accepted Manuscript

(81) Abrahams, S. C.; Kurtz, S. K.; Jamieson, P. B. *Phys. Rev.* **1968**, *172*, 551–553.
(82) Ablitt, C.; Craddock, S.; Senn, M. S.; Mostofi, A. A.; Bristowe, N. C. *Comput. Mater.* **2017**, *3*, 44.
(83) Olsen, R. B.; Bruno, D. A.; Briscoe, J. M. *J. Appl. Phys.* **1985**, *58*, 4709–4716.
(84) Maeda, Y.; Wakamatsu, T.; Konishi, A.; Moriwake, H.; Moriyoshi, C.; Kuroiwa, Y.; Tanabe, K.; Terasaki, I.; Taniguchi, H. *Phys. Rev. Appl.* **2017**, *7*, 034012.
(85) Wakamatsu, T.; Tanabe, K.; Terasaki, I.; Taniguchi, H. *Phys. Status Solidi - Rapid Res. Lett.* **2017**, *11*, 1700009.

Accepted Manuscript




Accepted Manuscript